

Pure spin current injection of single-layer monochalcogenides

Bernardo S. Mendoza,^{1,*} Lucila Juárez-Reyes,¹ and Benjamin M. Fregoso²

¹*Centro de Investigaciones en Óptica, León, Guanajuato 37150, México*

²*Department of Physics, Kent State University, Kent, Ohio 44242, USA*

(Dated: December 21, 2021)

We compute the spectrum of pure spin current injection in ferroelectric single-layer SnS, SnSe, GeS, and GeSe. The formalism takes into account the coherent spin dynamics of optically excited conduction states split in energy by spin orbit coupling. The velocity of spins is calculated as a function of incoming photon energy and angle of linearly polarized light within a full electronic band structure scheme using density functional theory. We find peak speeds of 250, 210, 180 and 154 Km/s for SnS, SnSe, GeS and GeSe, respectively which are an order of magnitude larger than those found in bulk semiconductors, e.g., CdSe and GaAs. Interestingly, the spin velocity is independent of the direction of polarization of light in a range of photon energies. Our results demonstrate that single-layer SnS, SnSe, GeS and GeSe are candidates to produce on demand spin-velocity injection for spintronics applications.

I. INTRODUCTION

There is increasing interest in attaining precise control of the spin of electrons at mesoscopic scales because it could lead to novel quantum computation platforms.^{1–4} Pure spin current (PSC), i.e., spin current with no associated charge current, could lead to more efficient quantum devices because a PSC does not produce joule heating. A PSC can be realized in the spin Hall effect,⁵ one photon absorption of light,^{6–8} or interference of two optical beams.^{9,10}

In contrast to the well-known spin Hall effect which occurs in the ground state of the material, optically induced PSC occurs in excited states of the material. Linearly polarized light injects carriers symmetrically into $\pm k$ conduction states in the Brillouin zone (BZ). Yet, the velocity and spin operators are odd under time reversal symmetry and hence there is no net charge current^{6,11,12} or spin density after summation over all the BZ.¹³ However, the spin current is even under time reversal and hence it does not vanish after summation over all the BZ. The optical PSC will manifest as a spatial separation of spin-up spin-down components or electrons. Optical PSC has been measured by pump-probe techniques in gallium arsenide (GaAs),^{14,15} aluminum-gallium arsenide (AlGaAs)¹⁵, Co₂FeSi,¹⁶ and ZnSe.¹⁷

A major problem in the field of spintronics is the very short spin relaxation time scales¹⁸ which makes it difficult to maintain coherence required for a spin current.^{19–22} For this reason we turn our attention to novel two-dimensional (2D) materials. 2D materials represent the ultimate scaling in thickness with mechanical, optical, and electronic properties that are unique relative to their bulk counterparts. For example, single-layer or 2D group-IV mono-chalcogenides GeS, GeSe, SnS, and SnSe are actively being investigated,^{23–33} due to their band gaps and large carrier mobilities suitable for optoelectronics. Monochalcogenides are centrosymmetric in the bulk but lack inversion symmetry in single-layer form, thus allowing the generation of nonlinear effects such as

optical PSC.

In this paper we show that 2D ferroelectric GeS, GeSe, SnS, and SnSe exhibit large optical PSC as measured by the spin velocity injection (SVI) to be defined below. We compute the spectrum of SVI as a function of photon energy and angle of linearly polarized light. We consider the case of the particles moving on the plane of the slab and spin pointing out of the slab. Monolayer SnS was recently experimentally realized,³⁴ and hence our theoretical results have direct experimental relevance for this material.

This paper is organized as follows. In Section II, we present the PSC theoretical formalism, showing the main expressions used to numerically implement PSC and SVI calculations. In Section III we describe the 2D monochalcogenide SnS, SnSe, GeS and GeSe structures and in Section V, we describe the results corresponding to the SVI spectra for the chosen structures. Finally, we summarize our findings in Section VI.

II. THEORY

In this section we follow the formalism of Ref. 8 and present only the main theoretical results. We consider free Bloch electrons subject to an external homogeneous electric field

$$\mathbf{E}(t) = \mathbf{E}(\omega)e^{-i\omega t} + c.c.. \quad (1)$$

The main idea is to extract an effective dynamics of spinors states $c'c$ in the conduction bands. The key approximations are (i) hole spins do not contribute to the current, (ii) the energy split between spinors c, c' is small compared with the energy difference between either of the spinors energy and any valence band, and (iii) the frequency of the optical field is much larger than the energy split between the spinors. The equation of motion

of the effective density matrix $\rho(\mathbf{k}; t)$ is,^{7,8}

$$\frac{\partial \rho_{cc'}(\mathbf{k}; t)}{\partial t} = \frac{e^2}{i\hbar^2} E^a(\omega) E^b(-\omega) \sum_v r_{cv}^a(\mathbf{k}) r_{vc'}^b(\mathbf{k}) \quad (2)$$

$$\times \left(\frac{1}{\omega - \omega_{c'v}(\mathbf{k}) - i0^+} - \frac{1}{\omega - \omega_{cv}(\mathbf{k}) + i0^+} \right),$$

with $\hbar\omega_n(\mathbf{k})$ the energy of the electronic band n at point \mathbf{k} in the irreducible Brillouin zone (IBZ), $|n\mathbf{k}\rangle$ is the Bloch state, $\omega_{nm}(\mathbf{k}) \equiv \omega_n(\mathbf{k}) - \omega_m(\mathbf{k})$, H_0 is the free Bloch Hamiltonian which includes the spin-orbit coupling (SOC) and $H_0|n\mathbf{k}\rangle = \hbar\omega_n(\mathbf{k})|n\mathbf{k}\rangle$. Here c, c' are time-reversed spinor states which are split in energy by SOC. The denominators clearly indicate the resonance coming from the absorption of a photon with energy $\hbar\omega$, as the electron goes from the valence state v to either of the quasidegenerate states c or c' . Latin superscripts indicate Cartesian coordinates and are summed over if repeated.

In this article, we focus on typical ultrafast experiments,^{15,17} for which one can ignore spin relaxation.⁶ Thus, we neglect the precession of the spins due to the spin splitting of the bands as the precession period is long compared to the momentum scattering time.³⁵ Therefore, the spin current operator is given by

$$\hat{K}^{ab}(\mathbf{k}) = \frac{1}{2}(\hat{v}^a(\mathbf{k})\hat{S}^b(\mathbf{k}) + \hat{S}^b(\mathbf{k})\hat{v}^a(\mathbf{k})), \quad (3)$$

where $\hat{v} = [\hat{\mathbf{r}}, H_0]/i\hbar$ is the velocity operator, $\hat{\mathbf{r}}$ is the position operator, $\hat{\mathbf{S}} = \hbar\hat{\boldsymbol{\sigma}}/2$ is the spin operator with $\hat{\boldsymbol{\sigma}}$ the Pauli spin matrices, and we allowed for the fact that in general \hat{v} and $\hat{\mathbf{S}}$ do not commute.

We compute the average of the spin current injection tensor $\hat{\mathbf{K}}(\mathbf{k})$ as

$$\dot{K}^{ab}(\omega) = \int \frac{d^3k}{8\pi^3} \sum_{cc'} \frac{\partial \rho_{cc'}(\mathbf{k}; t)}{\partial t} K_{c'c}^{ab}(\mathbf{k}), \quad (4)$$

where we used the closure relationship $|n\mathbf{k}\rangle\langle n\mathbf{k}| = 1$, and the integral is over the IBZ. Then, we write

$$\dot{K}^{ab}(\omega) = \mu^{abcd}(\omega) E^c(\omega) E^d(-\omega), \quad (5)$$

where

$$\mu^{abcd}(\omega) = \frac{\pi e^2}{\hbar^2} \int \frac{d^3k}{8\pi^3} \sum'_{vcc'} K_{cc'}^{ab}(\mathbf{k}) r_{cv}^c(\mathbf{k}) r_{vc'}^d(\mathbf{k}) \quad (6)$$

$$\times [\delta(\omega - \omega_{c'v}(\mathbf{k})) + \delta(\omega - \omega_{cv}(\mathbf{k}))],$$

is the tensorial response function that characterises the PSC. The prime symbol the sum means that c and c' are quasi-degenerate conduction states, and the sum only covers these states. Finally,

$$K_{cc'}^{ab}(\mathbf{k}) = \frac{1}{2} \sum_{l=v,c} (v_{cl}^a(\mathbf{k}) S_{lc'}^b(\mathbf{k}) + S_{cl}^b(\mathbf{k}) v_{lc'}^a(\mathbf{k})), \quad (7)$$

are the matrix elements of Eq. (3).

An important point is that both charge current and net spin density vanish and hence the current is a PSC. For linear polarization, the momentum distribution of carriers is even in $\pm\mathbf{k}$. Assuming time reversal symmetry, the velocity is odd in \mathbf{k} and hence charge (injection) current vanishes after summation over the whole BZ.¹³ Similarly, the spin matrix elements are odd in \mathbf{k} and so the net spin density vanishes. The spin current³ however, is even in \mathbf{k} and does not vanish under linearly polarized light. Note that PCS with linearly polarized light vanishes in the absence of SOC and that other definitions of the spin operator,³⁶ are also even under time reversal symmetry.

A. Spin velocity

To quantify the speed of the particles we define an effective charge velocity as^{6,8}

$$\frac{\hbar}{2} \dot{n}(\omega) \mathbf{v}^{ab}(\omega) \equiv \dot{K}^{ab}(\omega). \quad (8)$$

\mathbf{v}^{ab} gives the velocity of electrons along Cartesian direction a with spin polarized along Cartesian direction b . The carrier injection rate $\dot{n}(\omega)$ is⁷

$$\dot{n}(\omega) = \xi^{ab}(\omega) E^c(\omega) E^d(-\omega), \quad (9)$$

where

$$\xi^{ab}(\omega) = \frac{2\pi e^2}{\hbar^2 V} \int \frac{d^3k}{8\pi^3} \sum_{vc} r_{vc}^a(\mathbf{k}) r_{cv}^b(\mathbf{k}) \delta(\omega - \omega_{cv}(\mathbf{k})), \quad (10)$$

is related to the imaginary part of the linear optical response tensor by $\text{Im}[\epsilon^{ab}(\omega)] = 2\pi\epsilon_0\hbar\xi^{ab}(\omega)$.

The function $\mathbf{v}^{ab}(\omega)$ allows us to quantify two very important aspects of PSC. First, we can fix the spin along direction b and calculate the resulting electron velocity. Second, we can fix the velocity of the electron along a and study the resulting direction along which the spin is polarized. In this article we restrict to the first case of the spin polarized along z to take the advantage of the 2D nature of the chosen monochalcogenides, where the spin would then be polarized perpendicular to the plane of the structures, as seen in Fig. 1. To this end, we use an incoming linearly polarized light at normal incidence, and use the direction of the polarized electric field to control $\mathbf{v}^{ab}(\omega)$. Indeed, writing $\mathbf{E}(\omega) = E_0(\omega)(\cos\alpha\hat{\mathbf{x}} + \sin\alpha\hat{\mathbf{y}})$, where α is the polarization angle with respect to x , we obtain from Eq. 8 that

$$\mathbf{v}^{xz}(\omega, \alpha) = \frac{2}{\hbar} \frac{\mu^{xxxy}(\omega) \sin 2\alpha}{\xi^{xx}(\omega) \cos^2 \alpha + \xi^{yy}(\omega) \sin^2 \alpha}, \quad (11)$$

and

$$\mathbf{v}^{yz}(\omega, \alpha) = \frac{2}{\hbar} \frac{\mu^{yyxx}(\omega) \cos^2 \alpha + \mu^{yyyy}(\omega) \sin^2 \alpha}{\xi^{xx}(\omega) \cos^2 \alpha + \xi^{yy}(\omega) \sin^2 \alpha}, \quad (12)$$

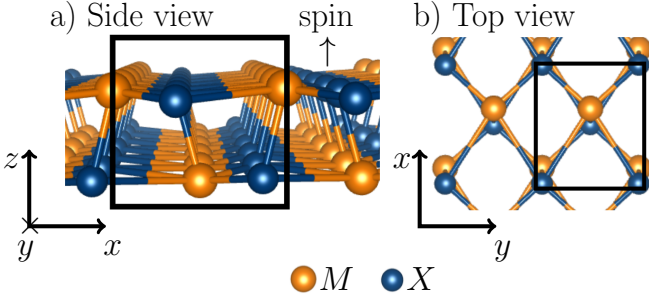


FIG. 1. (color online) The crystal structure of single-layer group-IV chalcogenides MX, where M=Ge, Sn, and X=S, Se. In a) we show the 3D view of the single-layer and in b) the projections of the single-layer crystal on the Cartesian axes. The black rectangles denotes the unit cell. The upward arrow denotes the z direction of the spin.

where $\mu^{xxzx}(\omega) = \mu^{xzyy}(\omega) = \mu^{yzxy}(\omega) = 0$ due to the $mm2$ point group symmetry of the chosen 2D monochalcogenides; we remark that only the $\mu^{azbc}(\omega)$ are involved for the spin polarized along z . The speed of the injected spin along z is given by

$$v^z(\omega, \alpha) = \sqrt{(v^{xz}(\omega, \alpha))^2 + (v^{yz}(\omega, \alpha))^2}, \quad (13)$$

that makes an angle $\theta^z(\omega, \alpha)$ with respect to x given by

$$\theta^z(\omega, \alpha) = \tan^{-1} \left(\frac{v^{yz}(\omega, \alpha)}{v^{xz}(\omega, \alpha)} \right). \quad (14)$$

We see that $v^{xz}(\omega, \alpha)$ and $v^{yz}(\omega, \alpha)$ have a mirror plane at $\alpha = 90^\circ$ and a period of 180° . We define the figure of merit for the speed of the injected spin along z by

$$v_a^z(\omega) = v^{az}(\omega, \alpha = \pi/4), \quad a = x, y. \quad (15)$$

III. STRUCTURES

Bulk monochalcogenide crystals MX (M = Ge, Sn and X = S, Se) are orthorhombic with point group mmm and space group $Pnma$ (No. 62). They consist of van der Waals-bonded double layers of metal monochalcogenide atoms in an armchair arrangement. The space group of the bulk crystal contains eight symmetries including a center of inversion which prevents pure spin current (PSC). Upon exfoliation, the resulting single “double layer” primitive cell has four atoms as seen in Fig. 1, with the layers chosen perpendicular to the z axis. The single-layer structure has four symmetries, including a two fold rotation with respect to x (plus translation), $2[001] + (1/2, 0, 1/2)$. In addition, the 2D system has two mirror symmetries with respect to z and y , $(1/2, 1/2, 1/2)$ and $m[010] + (0, 1/2, 0)$, that leads to an $mm2$ point group, which determines the nonzero components of the optical response tensors, like $\mu^{abcd}(\omega)$ and $\xi^{ab}(\omega)$. The atomic slab widths are 2.84, 2.73, 2.56 and 2.61 Å for SnS, SnSe, GeS, GeSe respectively.

IV. NUMERICAL METHOD

We calculated the self-consistent ground state and the Kohn-Sham states within density functional theory in the independent-particle scheme within the local density approximation (DFT-LDA), with a plane wave basis using the ABINIT.³⁷ The Hartwigsen-Goedecker-Hutter (HGH) relativistic separable dual-space Gaussian pseudopotentials,³⁸ are used to include the spin-orbit interaction needed to calculate K_{cc}^{ab} from Eq. 7. The convergence parameters for the calculations, for all the structures are a cutoff energy of 30 Ha, resulting in LDA band gaps of 1.35, 0.80, 1.82 and 1.05 eV for SnS, SnSe, GeS, GeSn, respectively. The TINIBA code,³⁹ was used to calculate the response functions for which 4356 \mathbf{k} points in the IBZ were used to integrate $\mu^{abcd}(\omega)$ and $\xi^{ab}(\omega)$ using the linearized analytic tetrahedron method.⁷ We neglect the anomalous velocity term $\hbar(\boldsymbol{\sigma} \times \nabla V)/4m^2c^2$, where V is the crystal potential, in \hat{v} of Eq. 3, as this term is known to give a small contribution to PSC.⁶ Therefore, $[\hat{v}, \hat{S}] = 0$, and Eq. 3 reduces to $\hat{K}^{ab} = \hat{v}^a \hat{S}^b = \hat{S}^b \hat{v}^a$. Finally, the prime in the sum of Eq. 6 is restricted to quasi-degenerated conduction bands c and c' that are closer than 30 meV to each other, which is both the typical laser pulse energy width and the thermal room-temperature energy level broadening.⁷ We include 20 valence and 40 conduction bands, which accounts for all allowed transitions up to 6 eV. To model the slabs we use supercells of 20 Å along z , which corresponds to vacuum larger than 17 Å, and renormalize our results to the atomic slab widths mentioned in the previous section, thus removing the vacuum as it must.

V. RESULTS

We present results for monolayer SnS, which was experimentally realized recently,³⁴ as a representative example of the four monochalcogenides studied. In the appendix we shows the results for SnSe, GeS and GeSe.

In Fig. 2, we show as a function of $\hbar\omega$, $\mu^{azbc}(\omega)$, $\xi^{aa}(\omega)$, and $v_{x,y}^z(\omega)$ of Eqs. (6), (10), and Eq. (15), respectively. The latter gives the figure of merit, for SnS for the SVI (spin-velocity injection), and remark that $\xi^{aa}(\omega)$ is a positive definite function. We only show the results in the visible range, where there are ample sources of devices to produce light of the required energy or its corresponding wavelength $\lambda(\text{nm}) = 1240/\hbar\omega(\text{eV})$. We see that $v_{x,y}^z(\omega)$, which is the central result of this article, has a rich structure as a function of $\hbar\omega$, and more importantly, reaches values around ± 100 Km/s, albeit not necessarily at the same energies; similar values of the SVI were predicted for hydrogenated graphene.⁸ Right at the energy gap, we see the onset of $\mu^{azbc}(\omega)$ and $\xi^{aa}(\omega)$, and correspondingly of $v_{x,y}^z(\omega)$. There are three energy regions where $v_{x,y}^z(\omega)$ are large, to wit, just below 1.6 eV in the Red subrange of the visible, between 2.0 and 2.2 eV covering Orange, Yellow and Green colors, and around 2.7 eV in the Blue.

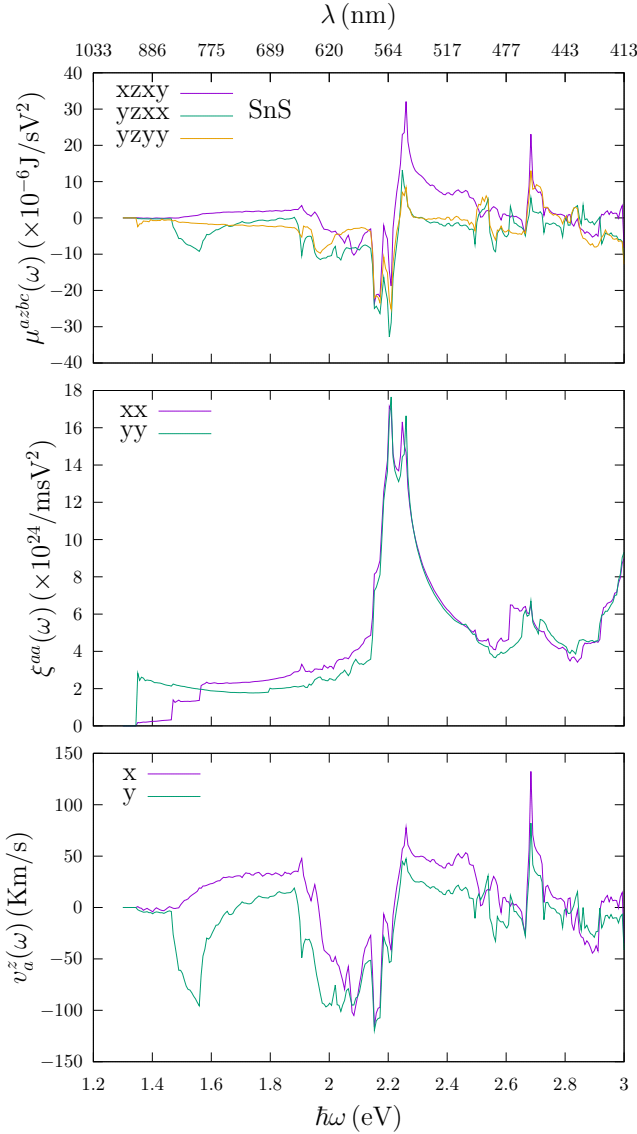


FIG. 2. (Color Online) $\mu^{azbc}(\omega)$, $\xi^{aa}(\omega)$, and $v_{x,y}^z(\omega)$ of Eqs. (6), (10), and (15) respectively, vs $\hbar\omega$ for SnS.

The behaviour of $v_{x,y}^z(\omega)$ vs. $\hbar\omega$ could be understood by looking at $\mu^{azbc}(\omega)$ and $\xi^{aa}(\omega)$ (upper panels). For instance, the structure of the large peak which leads to a negative $v_y^z(\omega)$ from 1.4 to 1.8 eV comes directly from $\mu^{yzxx}(\omega)$ as $\xi^{xx}(\omega)$ and $\xi^{yy}(\omega)$ have several featureless flat plateaus in that energy region. On the other hand, the structures of $v_x^z(\omega)$ and $v_y^z(\omega)$ between 2.0 and 2.2 eV and around 2.7 eV come from the interplay of the $\mu^{azbc}(\omega)$ and both $\xi^{xx}(\omega)$ and $\xi^{yy}(\omega)$, as prescribed by Eqs. (11) and (12) at $\alpha = \pi/4$.

We analyze the dependence of $v^z(\omega, \alpha)$ and $\theta^z(\omega, \alpha)$ (Eqs. (13) and (14)), with α , the angle that gives the direction of the linearly polarized electric field of the normally incident beam of light. To do so, we zoom into the three regions of $\hbar\omega$ mentioned above, for which we find not only a large value of the SVI but also an inter-

esting behavior that allows the manipulation of the direction of the SVI itself through the value of α . In Fig. 3 (left panel) we show $v^z(\omega, \alpha)$ and $\theta^z(\omega, \alpha)$ vs. α , for $\hbar\omega = 1.521, 1.534, 1.547$ and 1.559 eV, corresponding to the near infrared. We notice that for $\alpha = 0^\circ$, $v^z(\omega, \alpha)$ is maximum for the chosen values of $\hbar\omega$ and reaches speeds around 225 Km/s. As we move towards $\alpha = 90^\circ$, $v^z(\omega, \alpha)$ decreases smoothly and is close to 45 Km/s. Also, we see that at $\alpha = 0^\circ$ and 90° , $\theta^z(\omega, \alpha) = 270^\circ$, which can be easily understood as for these angles $v^{x,z}(\omega, \alpha) = 0$, and thus the spin velocity would be pointing towards $-y$, for an incoming polarization along x or y . Moreover, we notice that for the other values of α the spin velocity does not deviate much from the $-y$ direction. In the middle panel of Fig. 3, we show again $v^z(\omega, \alpha)$ and $\theta^z(\omega, \alpha)$ vs. α , but for $\hbar\omega = 1.951, 1.957, 1.964, 1.970$ and 1.983 eV, corresponding to the Red subrange of the visible. For these choices of $\hbar\omega$ we see that the variation of $v^z(\omega, \alpha)$ vs. α is smaller than from the previous cases and is non monotonic as a function of $\hbar\omega$. On the other hand the behavior of $\theta^z(\omega, \alpha)$ is monotonic for the new set of chosen values of $\hbar\omega$, and it displays a very interesting behavior for $\hbar\omega = 1.964$ eV for which $\theta^z(\omega, \alpha) = 270^\circ$, i.e. is constant as a function of α ; on top of this, we notice that the corresponding $v^z(\omega, \alpha) \sim 137$ Km/s, is also almost constant as a function of α . This means that regardless of the orientation of the polarization of the impinging electric field, the spin-velocity current will be directed along $-y$ with nearly a constant speed; we find a similar behaviour for SnSe (see the appendix). Therefore, there are energies of the incoming light for which one can inject z -polarized spins along the y surface direction regardless of the polarization angle α , thus opening the possibility of having SVI for unpolarized light.

Above behaviour is easily explained from Fig. 2, where for $\hbar\omega = 1.964$ eV, we see that as $\mu^{yzxx}(\omega) \sim \mu^{yzyy}(\omega) < 0$, $\xi^{xx}(\omega) \sim \xi^{yy}(\omega)$, and $\mu^{xzyy}(\omega) \sim 0$, then Eq. (12) will imply that $v^{yz}(\omega, \alpha)$ is almost independent of α , and Eq. (11) implies that $v^{xz}(\omega, \alpha) \sim 0$. Therefore, Eq. (14) gives $\alpha = 270^\circ$. Finally, in Fig. 3 (right panel), for $\hbar\omega = 2.659, 2.665, 2.678, 2.684$ and 2.690 eV, in the Blue region of the spectrum, we show again $v^z(\omega, \alpha)$ and $\theta^z(\omega, \alpha)$ vs. α . For $v^z(\omega, \alpha)$ we see a monotonic behaviour as a function of $\hbar\omega$, where $\alpha = 45^\circ$ maximizes the speed that could be as large as ~ 140 Km/s. Now, what is interesting to see is that the resulting SVI shows similar values of $\theta^z(\omega, \alpha)$ in the third quadrant for energies around (2.659, 2.665) eV and in the first quadrant for energies around (2.678, 2.690) eV.

Finally, we calculate the average distance d by which the up and down spin populations are displaced. From Ref. 6 we obtain that $d \sim 4\tau v^z(\omega, \alpha)$, where τ is the momentum relaxation time. For instance, assuming $\tau = 100$ fs,¹⁷ from Fig. 2 we see that $v^z(\omega, \alpha = 0) \sim 260$ Km/s for $\hbar\omega = 2.151$ eV and then $d \sim 104$ nm. This value of d is ~ 5 times larger than those experimentally measured values of $d = 20$ nm for GaAs/AlGaAs¹⁵ and $d = 24$ nm for ZnSe,¹⁷ making the SnS, SnSe, GeS and GeSe

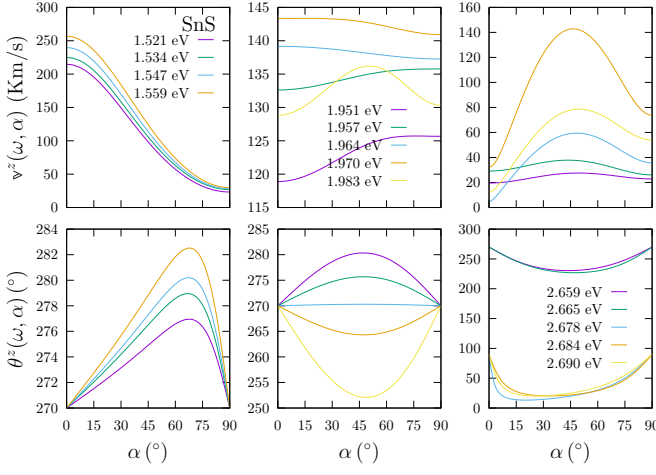


FIG. 3. (Color Online) $v^z(\omega, \alpha)$ and $\theta^z(\omega, \alpha)$ of Eqs. (13) and (14), respectively, vs. α for SnS.

monochalcogenides, excellent structures for the realization of PSC.

VI. CONCLUSIONS

Using novel single-layer 2D monochalcogenides, SnS, SnSe, GeS, and GeSe, we have shown that these 2D films are excellent candidates for spin current injection. In particular, we reported the results of *ab initio* calculations for the spin velocity injection (SVI) due to one-photon absorption of the linearly polarized light as a function of its energy and direction of polarization. The theoretical formalism to calculate the SVI includes the excited coherent superposition of the spin-split conduction bands that arise in the noncentrosymmetric structures considered here. We made the calculations for the cases when the spin is polarized in the z direction that is perpendicular to the 2D films and study the resulting SVI velocity along the x or y directions parallel to the films. We have shown that the SVI display an interesting behavior, which depends upon the material, but where we found

similarities in that all of them show values around and above 150 Km/s for the SVI, with an ample control of the direction of the SVI through the manipulation of the angle α of the linearly polarized light. Also, the particularities of each material made these structures excellent spintonic candidates. In particular we found that for SnS and SnSe there are energies of the incoming light for which one can inject z -polarized spins along the y surface direction regardless of the polarization angle α of the linearly polarized light, thus opening the possibility of having SVI for unpolarized light.

The speed values obtained here are of the same order of magnitude as those of Ref. 10 in unbiased semiconductor quantum well structures, and Ref. 8 in hydrogenated graphene structures, while they are an order of magnitude higher compared to 3D bulk materials. Moreover, the distance d by which the spin up and spin down populations are separated is larger than for other semiconductors where d has been measured.^{15,17} Therefore, the 2D monochalcogenide structures considered here are excellent candidates for the development of spintronics devices that require pure spin current (PSC).

VII. ACKNOWLEDGMENT

L.J.R. acknowledges support by CONACyT through a postdoctoral research fellowship. B.S.M. acknowledges the support from CONACyT through grant A1-S-9410. B.M.F. thank NSF DMR-2015639 and NERSC-DOE-AC02-05CH11231.

Appendix A: Results for SnSe, GeS and GeSe

We go over the results for SnSe, GeS and GeSe, which qualitatively are very similar to those presented for SnS in the main text. However, we point out only the most relevant features, since the detailed explanation could be done following that of SnS.

In Fig. 4 we show as a function $\hbar\omega$, for SnSe, GeS, and GeSe, $\mu^{azbc}(\omega)$, $\xi^{aa}(\omega)$, and $v_{x,y}^z(\omega)$ of Eqs. 6, 10, and Eq. 15, of the main text, respectively. We see that $v_{x,y}^z(\omega)$, for each structure has an interesting behaviour as a function of $\hbar\omega$, reaching maximum values around -150 , ± 100 , and -100 Km/s for SnSe, GeS and GeSe, respectively, each at different regions of $\hbar\omega$.

As for SnS, we identify three energy regions for each structure where $v_{x,y}^z(\omega)$ are large. For SnSe the $\hbar\omega$ regions are $[0.891, 0.931]$ and $[1.424, 1.454]$ eV, both in the

near infrared, and $[1.675, 1.735]$ eV in the Red subregion of the visible spectrum. Then, for GeS we have $\hbar\omega \sim [2.582, 2.622]$ eV in the blue, $[3.156, 3.177]$ eV in the violet, and $[3.460, 3.520]$ eV in the near UV. Finally, for GeSe we have $\hbar\omega \sim [1.713, 1.733]$ eV in the Red, $[1.984, 2.064]$ eV in the Orange, and $[2.485, 2.576]$ eV in the Blue. As explained for SnS, the features seen in $v_{x,y}^z(\omega)$ readily come from the interplay of $\mu^{azbc}(\omega)$ and $\xi^{aa}(\omega)$ shown in the upper panels of the corresponding figure for each system, from where they can be deduced

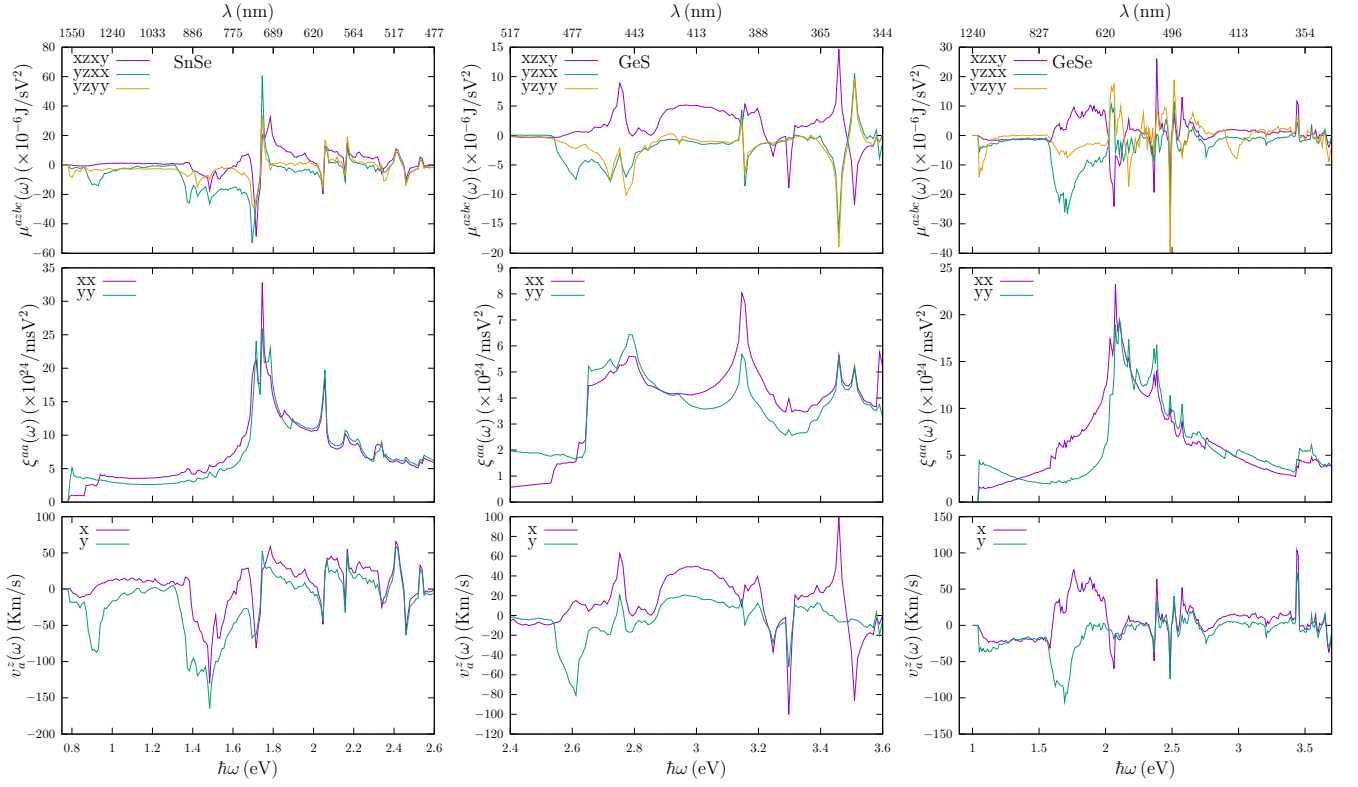


FIG. 4. (Color Online) $\mu^{abc}(\omega)$, $\xi^{aa}(\omega)$, and $v_{(x,y)}^z(\omega)$ of Eqs. 6, 10, 15 respectively, vs $\hbar\omega$ for SnSe, GeS and GeSe.

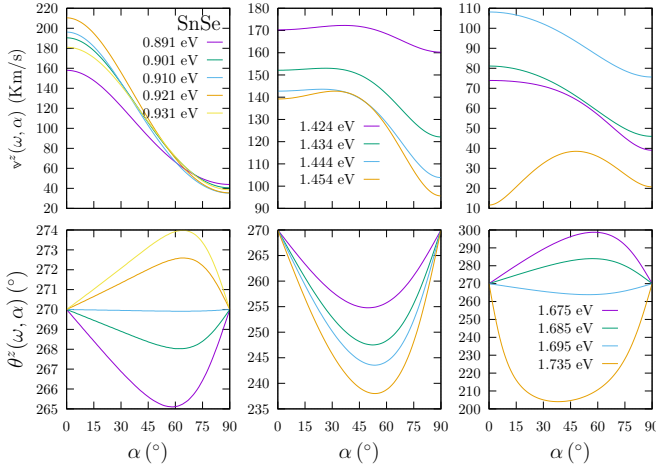


FIG. 5. (Color Online) $v^z(\omega, \alpha)$ and $\theta^z(\omega, \alpha)$ of Eqs. 13 and 14, respectively, vs. α for SnSe.

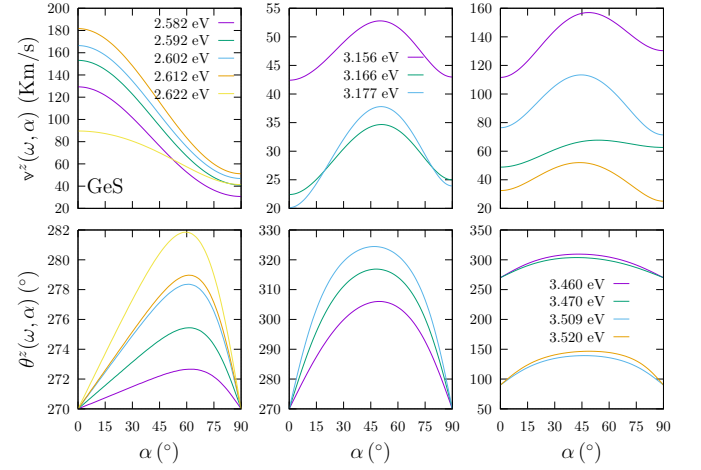


FIG. 6. (Color Online) $v^z(\omega, \alpha)$ and $\theta^z(\omega, \alpha)$ of Eqs. (13) and (14), respectively, vs. α for GeS.

in detail. (Eqs. 13 and 14 of the main text), vs. α , which is the angle that gives the direction of the linearly polarized electric field of the normally incident beam of light, also shows a very interesting behaviour for SnSe, GeS and GeSe, as shown in Figs. 5 for SnSe, 6 for GeS and 7 for GeSe, where each panel corresponds to the energy regions given in the previous paragraph for each system. We find very large values of the SOL and also an interesting behavior that allows the manipulation of

the direction of the SOL itself through the value of α , just as explained in the main text for SnS. For instance we see that for SnSe at 0.910 eV (Fig. 4), the direction of the resulting SOL $v^z(\omega, \alpha)$ (Eq. 15) of the main text is $\theta^z(\omega, \alpha) = 270^\circ$ independent of α , just as we obtained for SnS at 1.964 eV and shown in Fig. 2 of the main text. Also, for SnSe we see that for $\hbar\omega = 1.424$ eV $v^z(\omega, \alpha)$ is almost constant with a value of 165 Km/s, with a variation of $\theta^z(\omega, \alpha)$ close to the $-y$ direction. Going

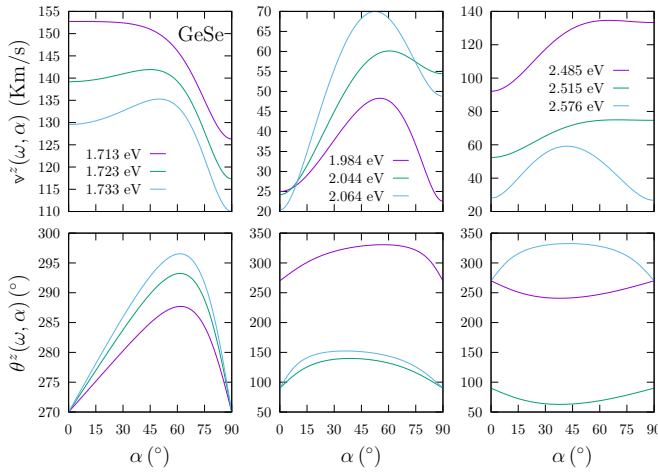


FIG. 7. (Color Online) $v^z(\omega, \alpha)$ and $\theta^z(\omega, \alpha)$ of Eqs. 13 and 14, respectively, vs. α for GeSe.

through the results of GeS and GeSe we can find similar behavior, and in general we see that the single-layer 2D monochalcogenides SnS, SnSe, GeS, and GeSe, offer a wide set of possibilities to manipulate with linearly polarized light the spin-velocity injection (SVI) of a pure spin current (PSC).

* E-mail: bms@cio.mx

- ¹ S. A. Wolf, D. D. Awschalom, R. A. Buhrman, J. M. Daughton, S. Von Molnar, M. L. Roukes, A. Y. Chtchelkanova, and D. M. Treger, *Science* **294**, 1488 (2001).
- ² D. D. Awschalom and M. E. Flatté, *Nat. Phys.* **3**, 153 (2007).
- ³ J. Fabian, A. Matos-Abiad, C. Ertler, P. Stano, and I. Zutic, *Ac. Phys. Slov.* **57**, 565 (2007).
- ⁴ D. D. Awschalom, D. Loss, and N. Samarth, *Semiconductor Spintronics and Quantum Computation* (Springer, Berlin; London, 2011).
- ⁵ J. Sinova, D. Culcer, Q. Niu, N. A. Sinitsyn, T. Jungwirth, and A. H. MacDonald, *Phys. Rev. Lett.* **92**, 126603 (2004).
- ⁶ R. D. R. Bhat, F. Nastos, A. Najmaie, and J. E. Sipe, *Phys. Rev. Lett.* **94**, 096603 (2005).
- ⁷ F. Nastos, J. Rioux, M. Strimas-Mackey, B. S. Mendoza, and J. E. Sipe, *Phys. Rev. B* **76**, 205113 (2007).
- ⁸ R. Zapata-Peña, B. S. Mendoza, and A. I. Shkrebtii, *Phys. Rev. B* **96**, 195415 (2017).
- ⁹ R. D. R. Bhat and J. E. Sipe, *Phys. Rev. Lett.* **85**, 5432 (2000).
- ¹⁰ A. Najmaie, R. D. R. Bhat, and J. E. Sipe, *Phys. Rev. B* **68**, 165348 (2003).
- ¹¹ S. F. Alvarado, H. Riechert, and N. E. Christensen, *Phys. Rev. Lett.* **55**, 2716 (1985).
- ¹² B. Schmiedeskamp, B. Vogt, and U. Heinzmann, *Phys. Rev. Lett.* **60**, 651 (1988).
- ¹³ B. M. Fregoso, *Phys. Rev. B* **100**, 064301 (2019).
- ¹⁴ H. Zhao, E. Loren, H. V. Driel, and A. Smirl, *Phys. Rev. Lett.* **96**, 246601 (2006).
- ¹⁵ M. J. Stevens, A. L. Smirl, R. D. R. Bhat, A. Najmaie, J. E. Sipe, and H. M. Van Driel, *Phys. Rev. Lett.* **90**, 136603 (2003).
- ¹⁶ T. Kimura, N. Hashimoto, S. Yamada, M. Miyao, and K. Hamaya, *NPG Asia Mat.* **4**, e9 (2012).
- ¹⁷ J. Hübner, W. W. Rühle, M. Klude, D. Hommel, R. D. R. Bhat, J. E. Sipe, and H. M. van Driel, *Phys. Rev. Lett.* **90**, 216601 (2003).
- ¹⁸ S. Murakami, N. Nagaosa, and S. C. Zhang, *Science* **301**, 1348 (2003).
- ¹⁹ S. Majumdar, R. Laiho, P. Laukkanen, I. J. Värynen, H. S. Majumdar, and R. Österbacka, *App. Phys. Lett.* **89**, 122114 (2006).
- ²⁰ S. Datta and B. Das, *App. Phys. Lett.* **56**, 665 (1990).
- ²¹ M. Götze, M. Joppe, and T. Dahm, *Scientific Reports* **6**, 36070 (2016).
- ²² Y. V. Pershin and M. Di Ventra, *Phys. Rev. B* **78**, 113309 (2008).
- ²³ L. Li, Z. Chen, Y. Hu, X. Wang, T. Zhang, W. Chen, and Q. Wang, *J. Am. Chem. Soc.* **135**, 1213 (2013).
- ²⁴ A. K. Singh and R. G. Hennig, *Appl. Phys. Lett.* **105**, 042103 (2014).
- ²⁵ F. Wang, S. M. Young, F. Zheng, I. Grinberg, and A. M. Rappe, *Nat. Commun.* **7**, 10419 (2016).
- ²⁶ P. Ramasamy, D. Kwak, D.-H. Lim, H.-S. Ra, and J.-S. Lee, *J. Mater. Chem. C* **4**, 479 (2016).
- ²⁷ M. Wu and X. C. Zeng, *Nano Lett.* **16**, 3236 (2016).
- ²⁸ C. Kamal, A. Chakrabarti, and M. Ezawa, *Phys. Rev. B* **93**, 125428 (2016).
- ²⁹ S.-D. Guo and Y.-H. Wang, *J. Appl. Phys.* **121**, 034302 (2017).
- ³⁰ C. Xin, J. Zheng, Y. Su, S. Li, B. Zhang, Y. Feng, and F. Pan, *J. Phys. Chem. C* **120**, 22663 (2016).
- ³¹ P. Z. Hanakata, A. Carvalho, D. K. Campbell, and H. S. Park, *Phys. Rev. B* **94**, 035304 (2016).
- ³² T. Rangel, B. M. Fregoso, B. S. Mendoza, T. Morimoto, J. E. Moore, and J. B. Neaton, *Phys. Rev. Lett.* **119**, 067402 (2017).
- ³³ B. S. Mendoza and B. M. Fregoso, *Phys. Rev. B* **102**, 195410 (2020).
- ³⁴ N. Higashitarumizu, H. Kawamoto, C.-J. Lee, B.-H. Lin, F.-H. Chu, I. Yonemori, T. Nishimura, K. Wakabayashi, W.-H. Chang, and K. Nagashio, *Nature Communications* volume **11** (2020).
- ³⁵ M. I. Dyakonov and V. I. Perel, *Modern Problems in Condensed Matter Sciences*, North-Holland, Amsterdam **8**, Chap. 2 (1984).
- ³⁶ J. Shi, P. Zhang, D. Xiao, and Q. Niu, *Phys. Rev. Lett.* **96**, 076604 (2006).
- ³⁷ X. Gonze, B. Amadon, P. M. Anglade, J. M. Beuken,

- F. Bottin, P. Boulanger, F. Bruneval, D. Caliste, R. Caracas, M. Côté, et al., Comput. Phys. Commun. **180**, 2582 (2009).
- ³⁸ C. Hartwigsen, S. Goedecker, and J. Hutter, Phys. Rev. B **58**, 3641 (1998).
- ³⁹ B. S. Mendoza, S. M. Anderson, J. L. Cabellos, and T. Rangel, *TINIBA: Ab initio calculation of the optical properties of solids, surfaces, interfaces, and 2D materials* (INDAUTOR-México No. 03-2009-120114033400-01, 2011).